Advanced Energy Systems, Inc.
27 Industrial Blvd, Unit E
Medford, NY 11763

Mr. Tom Schultheiss

Gridded thermionic gun and integral superconducting ballistic bunch compression cavity Phase I Final Report

Topic 24: Nuclear Physics Accelerator Technology

Subtopic d: Particle Beam Sources and Techniques

Phase I grant Award Number: DE-SC0013275

Identification and Significance of the Problem or Opportunity

Electron-Ion colliders such as the **M**edium energy **E**lectron **I**on **C**ollider (MEIC) being developed by JLAB require high current electrons with low energy spread for electron cooling of the collider ring. Accelerator techniques for improving bunch charge, average current, emittance, and energy spread are required for Energy Recovery Linacs (ERLs) and Circulator Rings (CR) for next generation colliders for nuclear physics experiments. Example candidates include thermionic-cathode electron guns with RF accelerating structures. Thermionic cathodes are known to produce high currents and have excellent lifetime. The success of the IR and THz Free-Electron Laser (FEL) designed and installed by Advanced Energy Systems at the Fritz Haber Institute (FHI) of the Max Planck Society in Berlin [1,2] demonstrates that gridded thermionic cathodes and rf systems be considered for next generation collider technology.

In Phase 1 Advanced Energy Systems (AES) developed and analyzed a design concept using a superconducting cavity pair and gridded thermionic cathode. Analysis included Beam Dynamics and thermal analysis to show that a design of this type is feasible. The latest design goals for the MEIC electron cooler were for electron bunches of 420 pC at a frequency of 952.6 MHz with a magnetic field on the cathode of 2kG. This field magnetizes the beam imparting angular momentum that provides for helical motion of the electrons in the cooling solenoid. The helical motion increases the interaction time and improves the cooling efficiency. A coil positioned around the cathode providing 2kG field was developed. Beam dynamics simulations were run to develop the particle dynamics near the cathode and grid. Lloyd Young added capability to Tstep to include space charge effects between two plates and include image charge effects from the grid. He also added new pepper-pot geometry capability to account for honeycomb grids. These additions were used to develop the beam dynamics for this gun. The general design is a modified ballistic compression cavity pair with two independently powered cells [3]. The first is a cathode cell that includes the thermionic cathode and grid to provide for beam bunching. The second is a full cell with independent phasing and field levels designed to minimize energy spread. The primary goal for Phase II is to manufacture a superconducting gun with a thermionic cathode and imbedded coil.

The system developed here is applicable to many high current electron accelerators. The analysis and design constraints imposed by the magnetized cathode make the cathode system developed here more complicated and limited than one without the magnetized beam constraints. High power ERLs would benefit by a gun with the capabilities shown here, 400 mA or more of current. ERLs hold great promise for electron cooling experiments, advanced light sources and Free Electron Lasers. This high current electron injector is a technological advance that will place the requirements for an ERL capable of providing quality bunches needed for cooling within the MEIC circulator ring within reach. This injector would have application to future ERLs around the world.

Technical Approach

High-average-current cathodes that deliver 420 pC of charge at 476.3 MHz for electron cooling in MEIC are long term technology goals proposed by JLAB [4]. JLAB studies have shown significant cost reduction if the frequency for the electron cooler is changed to 972.6 MHz. A

thermionic room temperature RF gun is being developed at BINP to replace the DC gun to improve cathode lifetime and provide higher current [5,6]. The gridded thermionic cathode and superconducting cavity developed here is a technology advance that can provide requirements needed for MEIC cooling and high current ERLs. Figure 1 shows the general layout of the first SRF cavity with the imbedded thermionic cathode. The upper left of the figure shows the gun concept that includes a thermal transition section between 2K and room temperature. This section is similar to what is used in SNS power couplers, 5K 3 atm helium input on the SRF side. Details of the helium requirements are shown later with the thermal results. The upper right of the figure shows a section cut. We use a coaxial feed as shown since this method results in a lower sensitivity to frequency and coupling from the position of the cathode. Two RF feeds are required, analysis showed that a single feed moved the field axis off the geometry center. The lower left shows the coil imbedded in the cathode stalk. The lower right shows the grid that was used in these analyses.

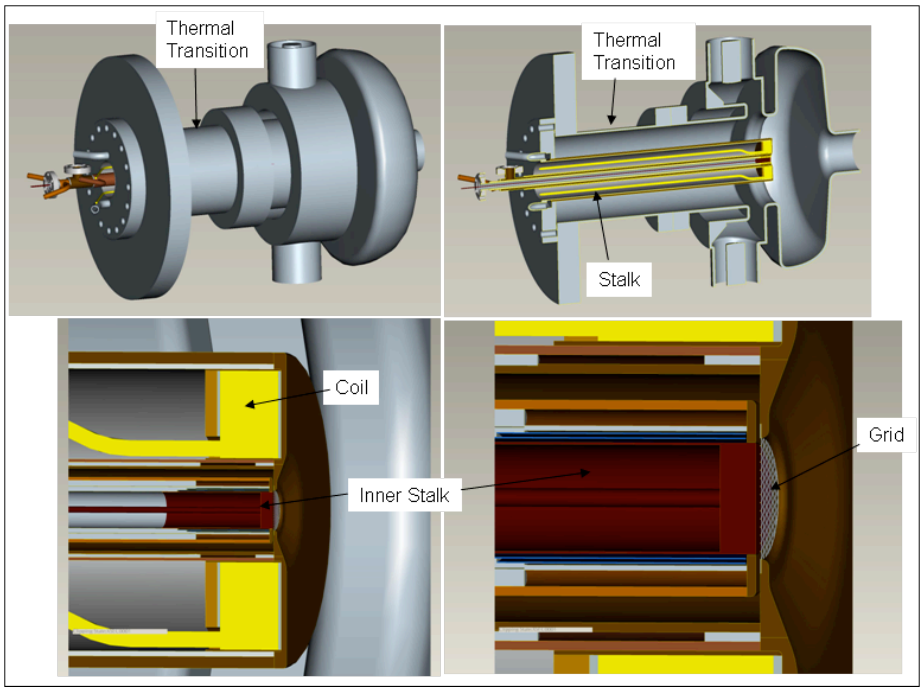

Figure 1, General Layout of SRF Gun and imbedded cathode

Details of the cathode stalk are shown in figure 2. The left of the figure shows the stalk with the solenoid coil. The outer jacket of the stalk is a copper tube with ribs machined along the length. These ribs add cooling area to enhance cooling and to absorb the high RF heat loads near the cavity. On the right of the figure is the cathode and grid region of the stalk. Grid RF is provided with an annular feed to the opening between the cathode and grid. The grid RF is from two frequencies, 952.6 MHz, a frequency that matches the RF input frequency to the cavity and its third harmonic, 2857.8 MHz. Overlaying the two frequencies at different phases shortens the bunch of electrons that pass through the grid to the main accelerating field. Thermal shields surround the cathode which will run to near 1000ºC. The cathode is biased to -480 volts and is thermally and electrically isolated from thermal shields and cooling tubes. Details of the local geometry and materials will be worked out in Phase II with HeatWave Labs. HeatWave has made cathodes with these requirements in the past.

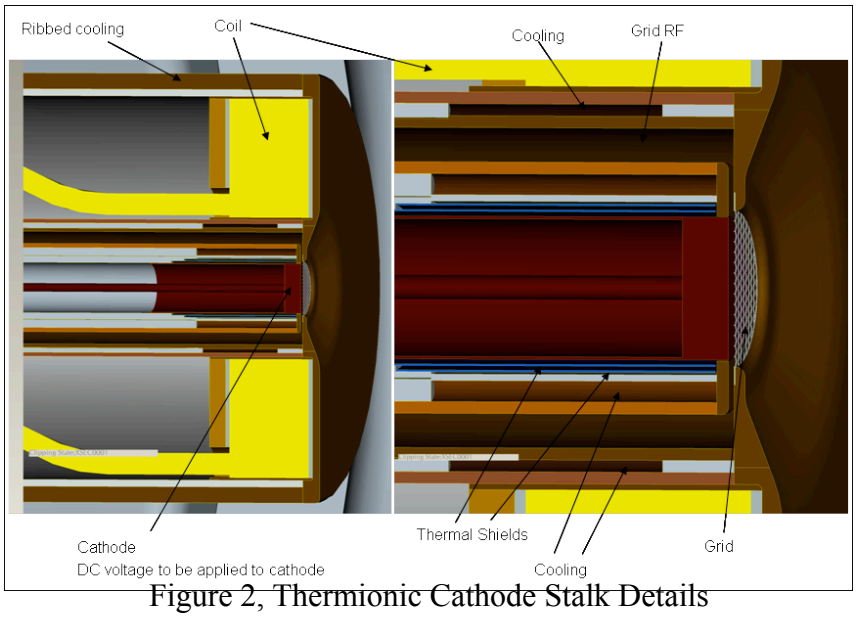

Figure 2, Thermionic Cathode Stalk Details

RF, Electrostatic, and Magnetic Analysis to Develop Fields

Prior to running beam dynamics the fields were developed. Three dimensional fields are needed between the cathode and grid for the two rf inputs in the inner coax, for the biased voltage set from the cathode and for the leakage field that enters through the grid from the cavity. These fields are needed from that cathode through the grid and to 1 mm from the cathode. The grid surface is located .25 mm from the cathode and is 50.8 μm thick. After 1mm from the cathode the fields become axisymmetric and SUPERFISH was used to generate the main cavity fields. Figure 3 shows the 3-D RF geometry of the gun and second cavity on the left. The RF geometry includes the details of the space set up by the grid honeycomb, shown on the right. RF analysis included external ports at the cavity RF feeds and at the inner RF feeds as shown.

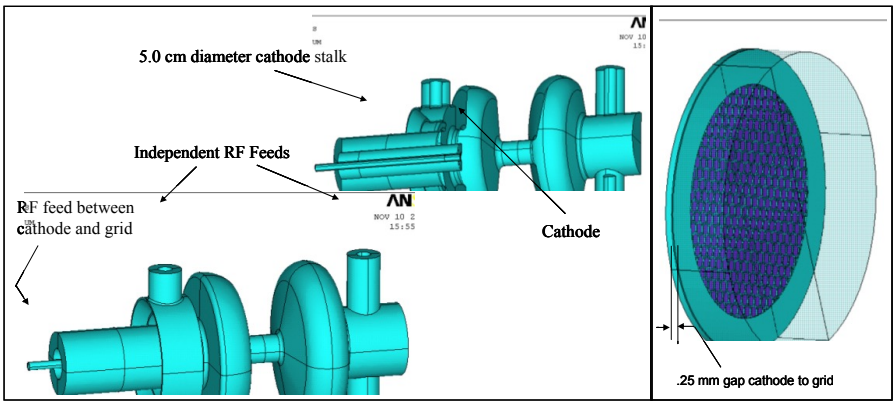

Figure 3, RF model geometry and RF ports

The next few figures show the fields that were developed for beam dynamics and for thermal analysis. The electric field from the RF input to the cavity at 952.6 MHz is shown in figure

4. On the right of the figure the local grid region is shown. Over one million elements were used to develop the fields with the majority near the grid. Figure 5 shows the magnetic fields from the cavity RF, they are used in beam dynamics and for thermal analysis.

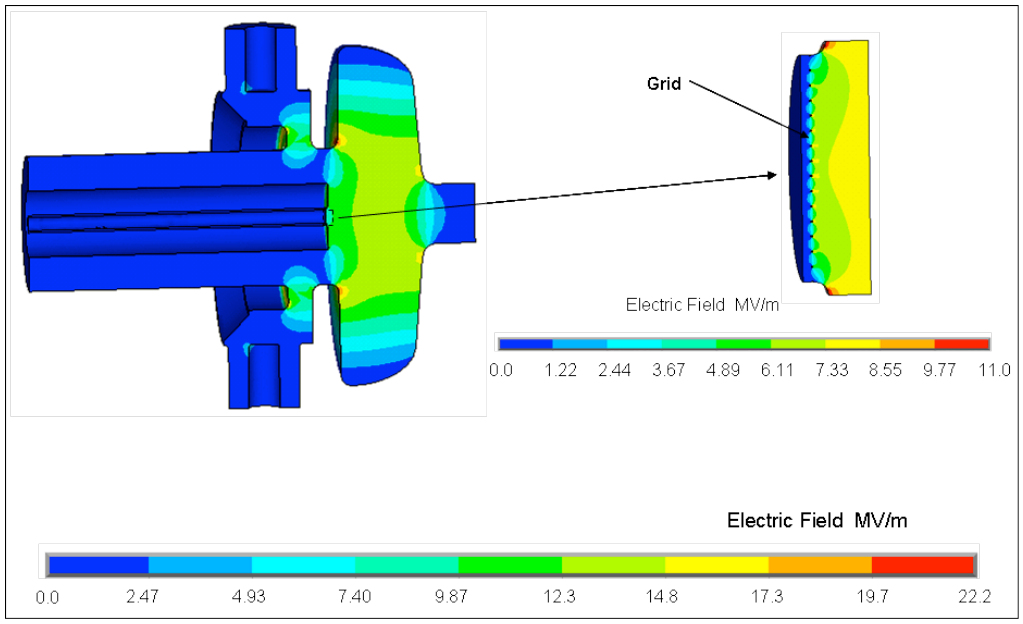

Figure 4, Electric Field From Cavity RF

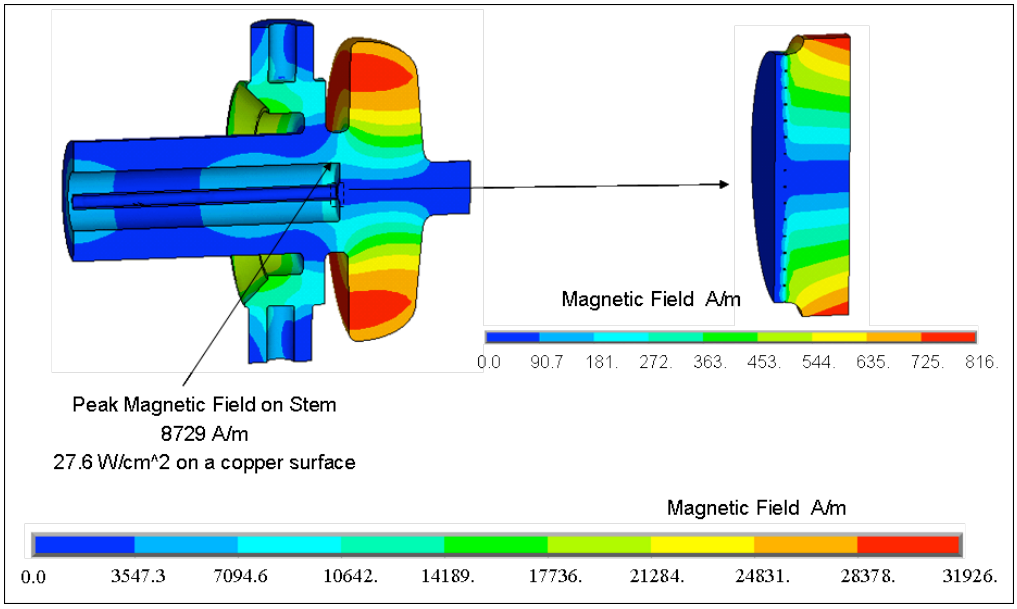

Figure 5, Magnetic Field From Cavity RF

Figures 6 and 7 show the electric fields near the cathode and grid for each of the RF inputs. Figure 6 shows that the leakage field on the cathode is about 10% of the field in the cavity. These values are comparable to the fields from the RF input through the inner coax, figure 7, and show that all three must be considered for beam dynamics.

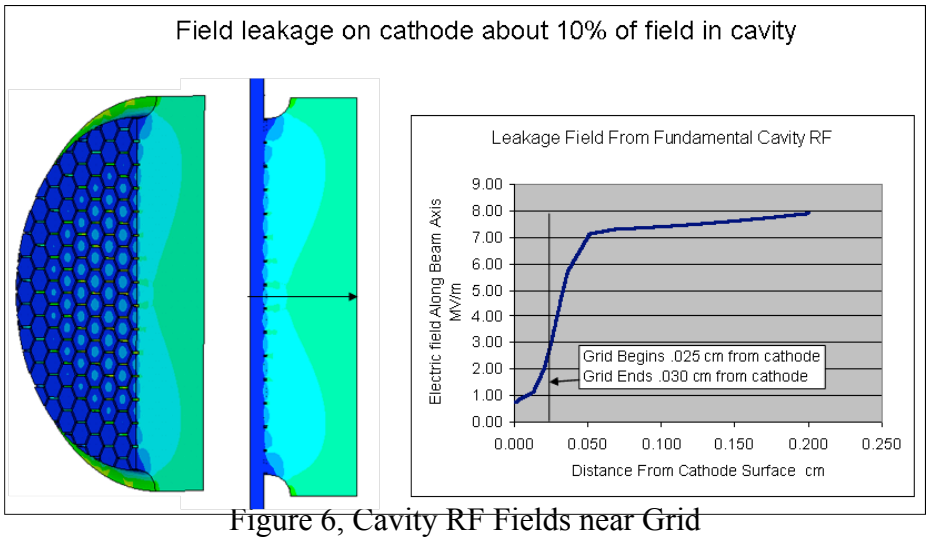

Figure 6, Cavity RF Fields near Grid

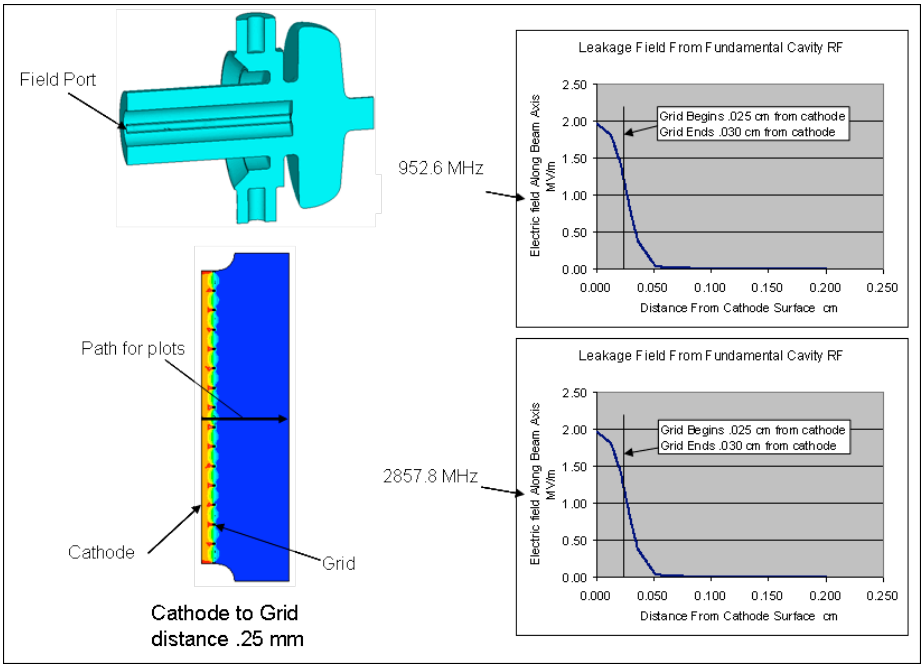

Figure 7, Inner RF Fields near Grid

The electrostatic fields were developed using the same RF model nodes and element connectivity but using an element with voltage as the degree of freedom. The cathode was set to negative 480 volts and the rest of the gun surfaces were set to ground (0 volts) including the grid. The resulting electric fields near the cathode and grid are shown in figure 8.

The magnetic fields from the coil are shown in figure 9. This requirement within the superconducting cavity increased the complexity of the cathode stalk significantly. The coil in limited space within a superconducting cavity has to provide 2kG on the cathode and at the same time an insignificant field on the superconducting material. The geometry of the coil also affects the geometry of the cavity facing surface since we wanted to limit the radial field on the cathode face. The stem's cavity facing geometry can be seen in figure 9. The coil is positioned so that the

cathode is within 1 cm of the coils edge limiting the radial field to 24 G at 3 mm cathode radius. If we were to move the coil to center the cathode the accelerating field from the main cavity would decrease significantly.

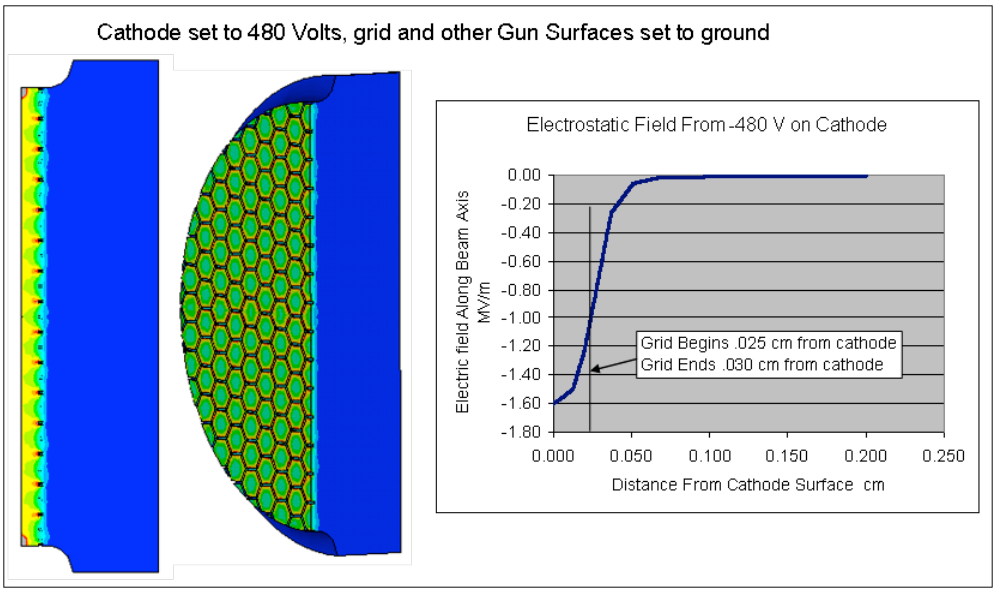

Figure 8, Electrostatic Fields Near the Grid

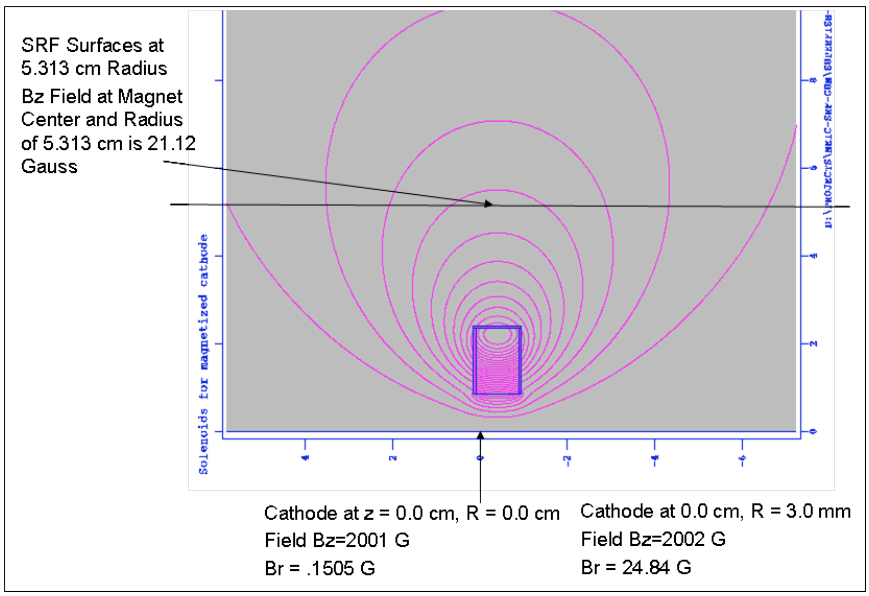

Figure 9, Magnetic Fields from Coil

The coil geometry was developed as a compromise between the radial field at the cathode and coil design limitations. Figure 10 shows the coil internal design evaluation. Since this coil requires a very high current density 32 A-T/mm^2 typical design methods will not work. For example, insulated wire turns will overheat due to poor thermal conductivity through the wire and insulation. However, if copper foil is used high currents are acceptable since power loss can be

conducted out through iron and into copper plates. Figure 10, shows the internal design calculations of a coil made of copper foil along with the equivalent thermal conductivities (axial and radial). This coil produces 422 watts of internal power loss that is included in the thermal analysis. AES will be working with a vendor in Phase II to develop the details of the coil. This vendor has made coils from copper foil.

Solenoid Requirement	
Field at Cathode kG	2
Cathode size mm	6
sheet thick with insulation inches	0.005
sheet thick no insulation	0.003
Router cm	2.3007
Rinner cm	0.8600
length cm	1
radial number of turms	113
length turns	1
number of turns	113
current amps	40.80
number of amp-turns	4610.17
permeability	1.257E-06
Current density A-T/m^2	3.200E+07
Current density A-T/mm^2	32.000
ave radius cm	1.5803
total foil length m	11.2204
Electrical Conductivity S/m	5.81E+07
foil area m^2	7.620E-07
resistance ohms	2.53E-01
resistance ohm/km	2.26E+01
voltage	1.03E+01
Power loss watts	4.22E+02
Power Density loss W/cm^3	29.489

Kapton insulation	
Insulation Therm Cond W/m-K	0.46
Copper Therm Cond W/m-K	300
x insulation meters .001" each side	0.0000508
x copper meters	0.0000762
equiv Thermal Cond rad W/m-K	1.147
equiv Thermal Cond rad W/cm-K	0.011
equiv Thermal Cond axial W/m-K	180.184
equiv Thermal Cond axial W/cm-K	1.80184

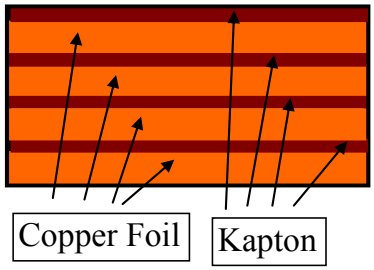

Figure 10, Copper Coil Evaluation

Beam Dynamics

TStep was modified to calculate the space charge between the cathode and grid plus calculate the space charge on the beam particles after leaving the grid. The image charge is included for both the cathode and grid for particles between the cathode and grid and for particles that have passed the grid.

The original problem had the specifications shown in Figure 11. But the latest requirements up the Frequency to 952.6 MHz with the same bunch charge. So the current requirement is now 400 mA.

When trying to simulate this gun with TStep we found that we could not get enough current with reasonable grid bias voltage and RF voltage applied between cathode and grid. The space charge was limiting the current when the effect of the grid on the space charge was ignored. Lloyd Young modified the 3d space charge routine to calculate the space charge between two parallel plates for the particles between the cathode and grid, plus calculate the space charge on particles

that have passed the grid including the image charge on the grid. A couple of assumptions are that the particles are not relativistic between the cathode and grid and that the grid is a perfectly conducting flat surface. The rf fields are calculated with a 3d code and imported into TStep. To view these RF fields, new diagnostics were added to TStep.

Bunch length	100 ps (3 cm)
Repetition rate new 952.6 MHz	476 MHz
Bunch charge	420 pC
Peak current	4.2 A
Average current new 400 mA	200 mA
Transverse normalized emittance	10s microns
Emitting radius (a_0)	3 mm
Solenoid field at cathode (B_z)	2 kG

Figure 11, the original specifications for the superconducting gridded gun injector.

The short pulse length 50 ps at 952.6 MHz require the RF applied to the space between the cathode and grid to be at least the 3rd harmonic or 2857.8 MHz. This is superimposed on 952.6 MHz RF fields also applied between the cathode and grid plus 952.6 MHz leakage through the grid from the superconducting cavity. Figure 12 shows the contribution of each of these three RF sources plus the static electric field from the grid bias. Ez 1 is RF applied to the space between the grid and cathode. As you can see in this plot it is nearly equal in magnitude and opposite in phase to the leakage from the RF fields in the superconducting cavity Ez 3. The third harmonic RF field Ez 2 applied to the grid is equal in magnitude to Ez 1 with the phase adjusted so that the total electric field is going negative just after the RF field in the superconducting cavity is turning positive to accelerate the electrons emerging from the grid. Thus for practically the whole time the voltage is positive for accelerating electrons from the cathode to grid, the fields in the main accelerating cavity are not in the correct direction to accelerate the electrons. The fields are all plotted in MV/m. The grid bias for this voltage is -480 volts.

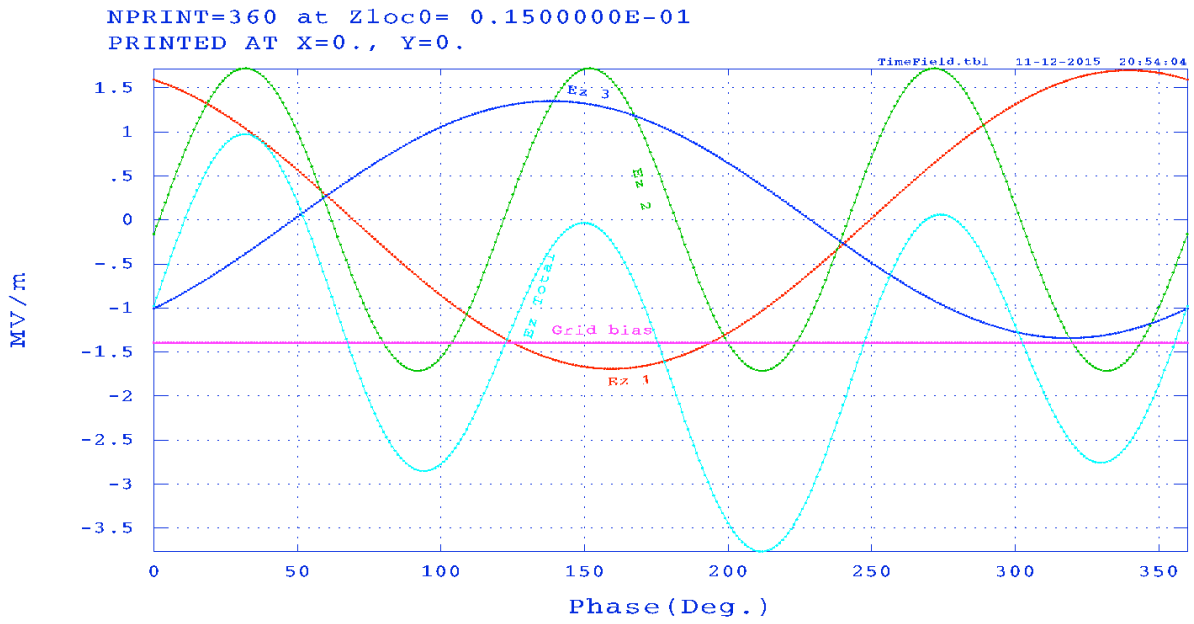

Figure 12, Total grid voltage and it's components for on period of the fundamental RF source.

Figure 13 shows a snap shot of the electron positions and kinetic energies at the RF phase of 50 degrees. This is just when the cavity is ready to accelerate the electrons. The fields between the grid and cathode are high enough to accelerate some electrons into the cavity even when the fields are in the reverse direction for acceleration. Thus the electrons get a certain amount of bunching. This bunching shortens the length of the accelerated bunch. In this figure, all the electrons to the left of zero are particle waiting to be injected into the problem. The cathode is a z equal to zero. The grid is located at 0.03 cm. The electrons are all within 0.2 cm of the grid at this phase of the RF. Figure 14 is at the same phase as Figure 13 with just change of perspective and scale. The reference particle is now in the center of the z scale. Figure 15 is show with same scales as Figure 14, but at a phase of 80 degrees. The Bunch being accelerated is pretty well formed at this stage. Note the effect of the grid on particles streaming through the grid, especially in the x vs z position plot.

Figure 16 shows the phase space of particles injected into the problem. This represents the beam at the cathode. Figure 17 shows the beam as it hits the grid at z=0.03 cm and figure 18 shows the phase space after the particles that hit the grid are removed at z=0.03 cm. Note that 26% of the beam is being intercepted by the grid. Also note that some beam is passing through the grid at an earlier time than the main pulse. This is caused by the total grid bias shown in Figure 12 is slightly positive at a phase of about 275 degrees. These particles are emerging from the grid at a phase where they cannot be accelerated by the fields in the superconducting cavity. Figure 19 shows the phase space at 1 cm from the cathode and Figure 20 shows the phase space at the end of the first superconducting cavity. The beam current at end of the first superconducting cavity is 0.44195 Amp with an average energy = 0.60563 MeV.

Figure 21, 22, and 23 show phase space plots at the exit of the grid, at z=1 cm and at the end of the first superconducting cavity. At the exit of the first cavity the emittance is about 13 cm-mrad rms normalized. If the solenoidal 2 kgauss field is turned off the emittance is only 2 cm-mrad rms normalized. So presumably the emittance would be about 2 cm mrad when the beam is back in a 2

kgauss solenoidal field. This emittance is about twice the requirement in the specification.
The beam is getting big at the end of the first superconducting cavity and without some focusing before the second superconducting cavity the beam would likely be large enough that some beam would be lost in the second cavity. Focusing would also likely reduce the emittance.

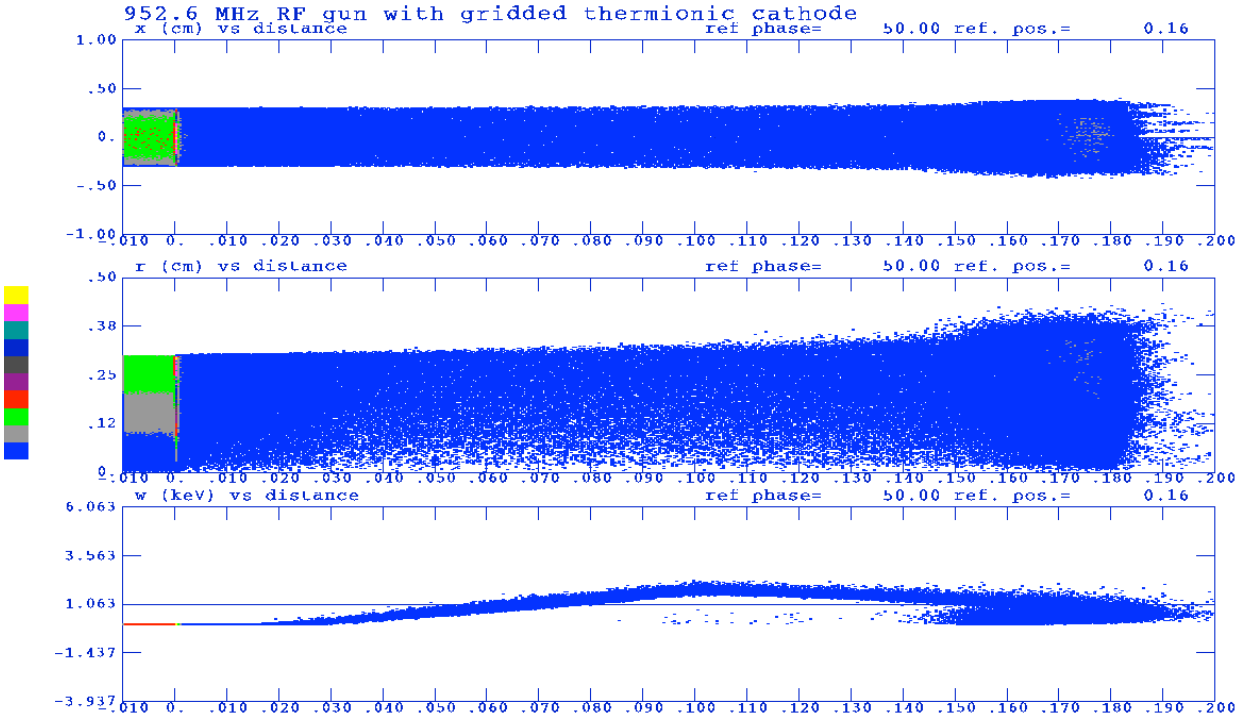

Figure 13 a plot of x and r positions and kinetic energies of the electrons injected into the accelerator. The dimensions are cm for x, r, and z positions. keV for the energy with respect to the reference particle located at a z position of 0.16 cm.

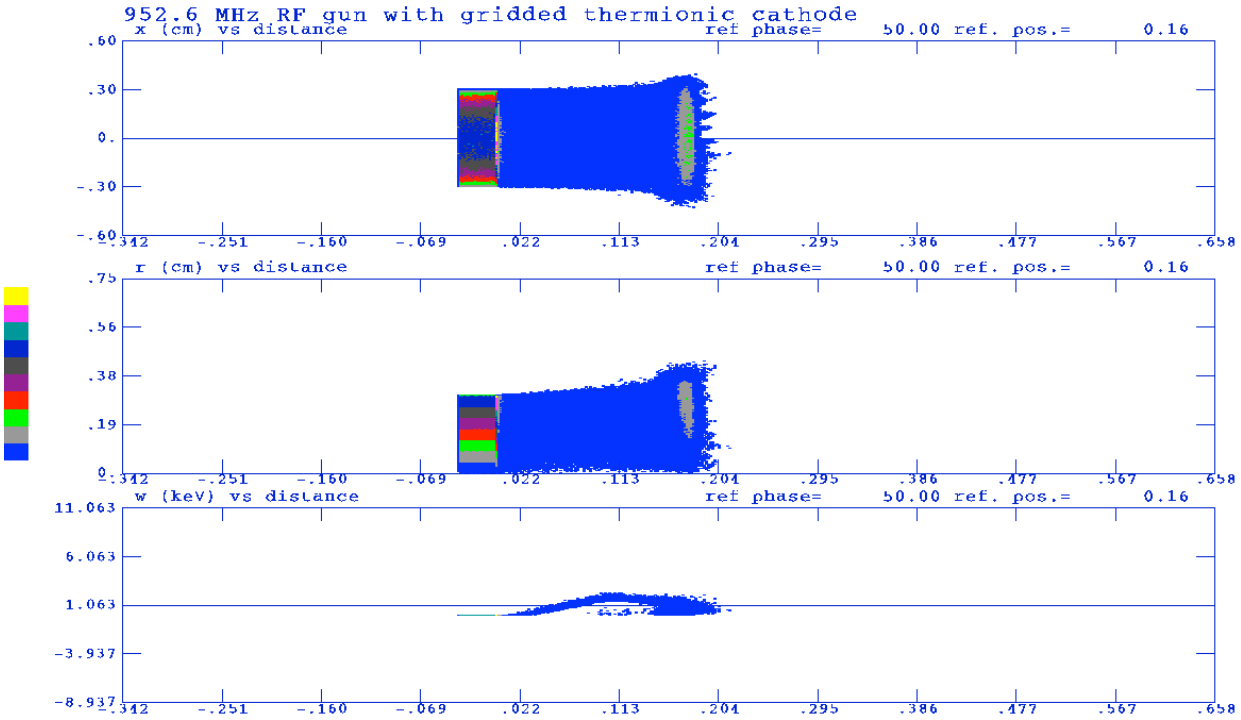

Figure 14 a snap shot of the beam at phase of 50 degrees. Z scale is centered on reference particle.

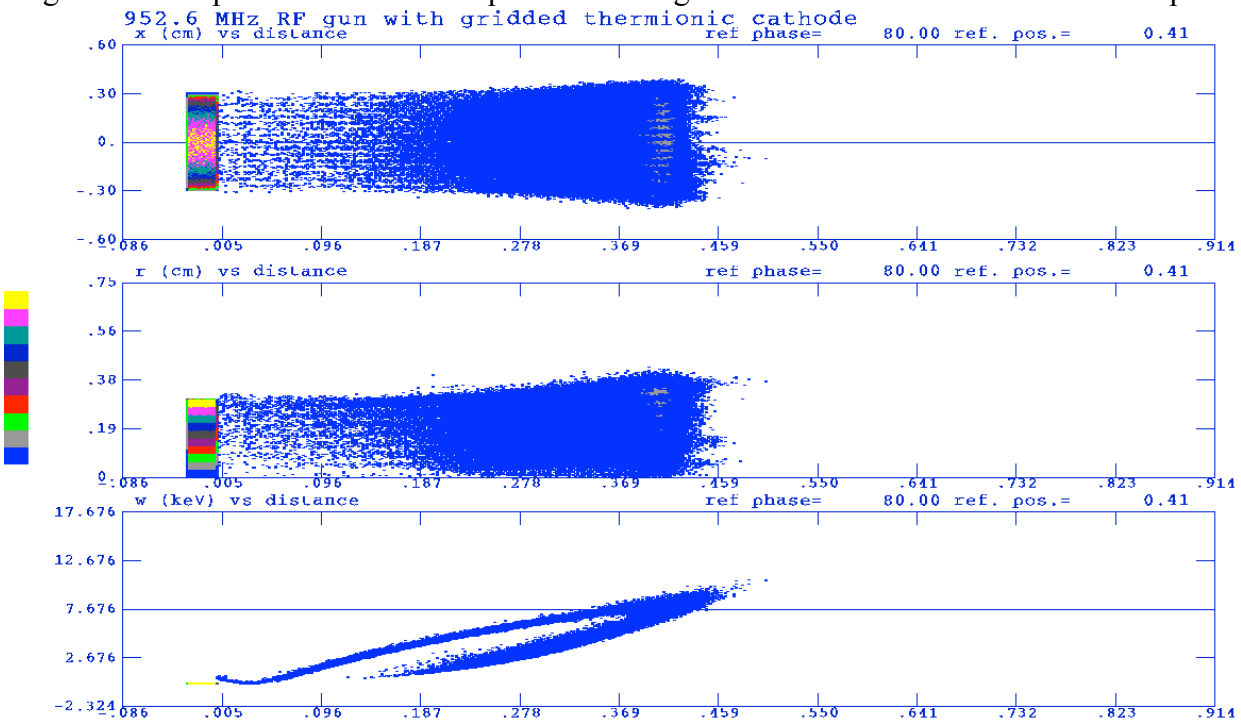

Figure 15 snap shot of electron positions at phase of 80 degrees. Some particles between grid and cathode at z positions less than 0.03 cm with energies slightly higher than the particles waiting to be injected are being accelerated toward the cathode.

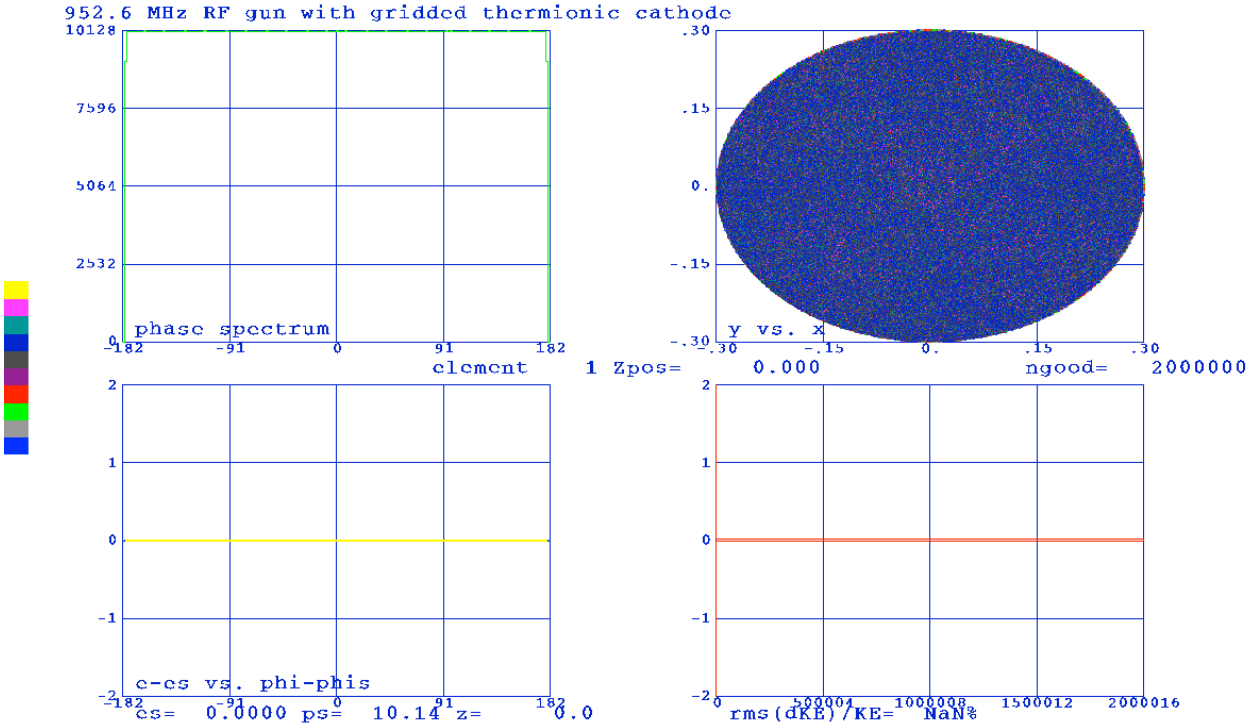

Figure 16 phase and energy spectrum of electrons emerging from cathode. Units are cm, particle count, and keV.

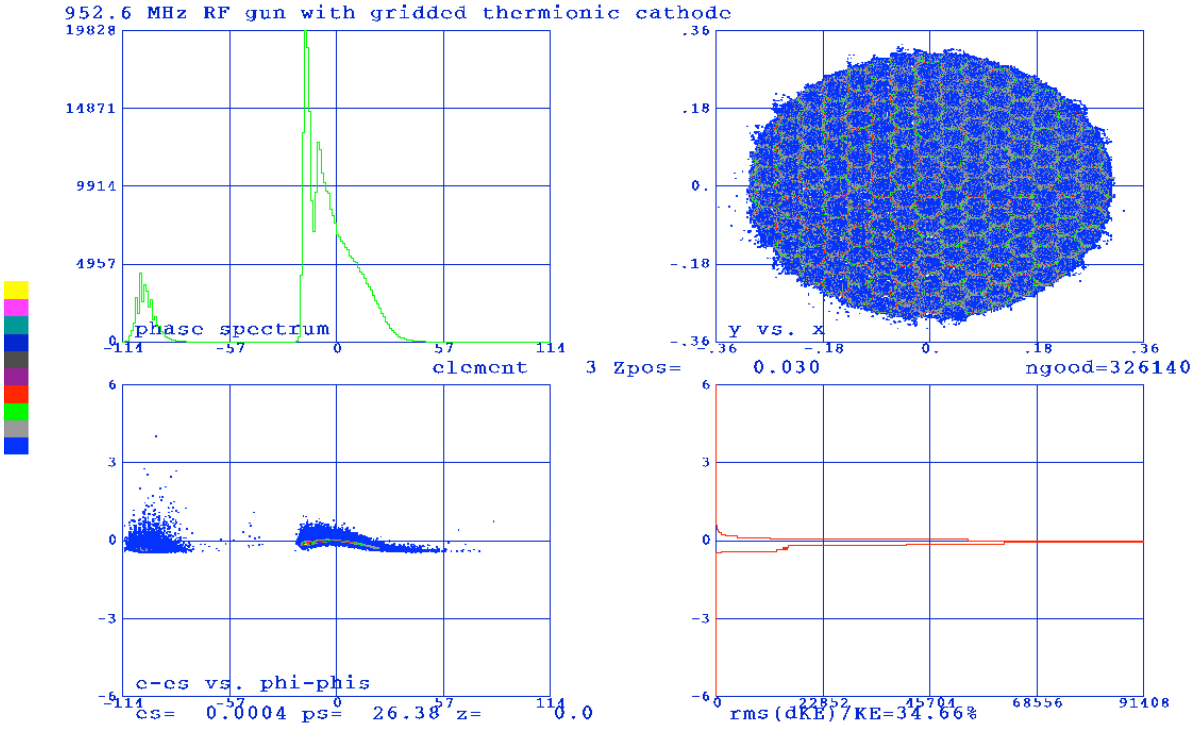

Figure 17 phase and energy spectrum at grid before particles are removed that hit the grid.

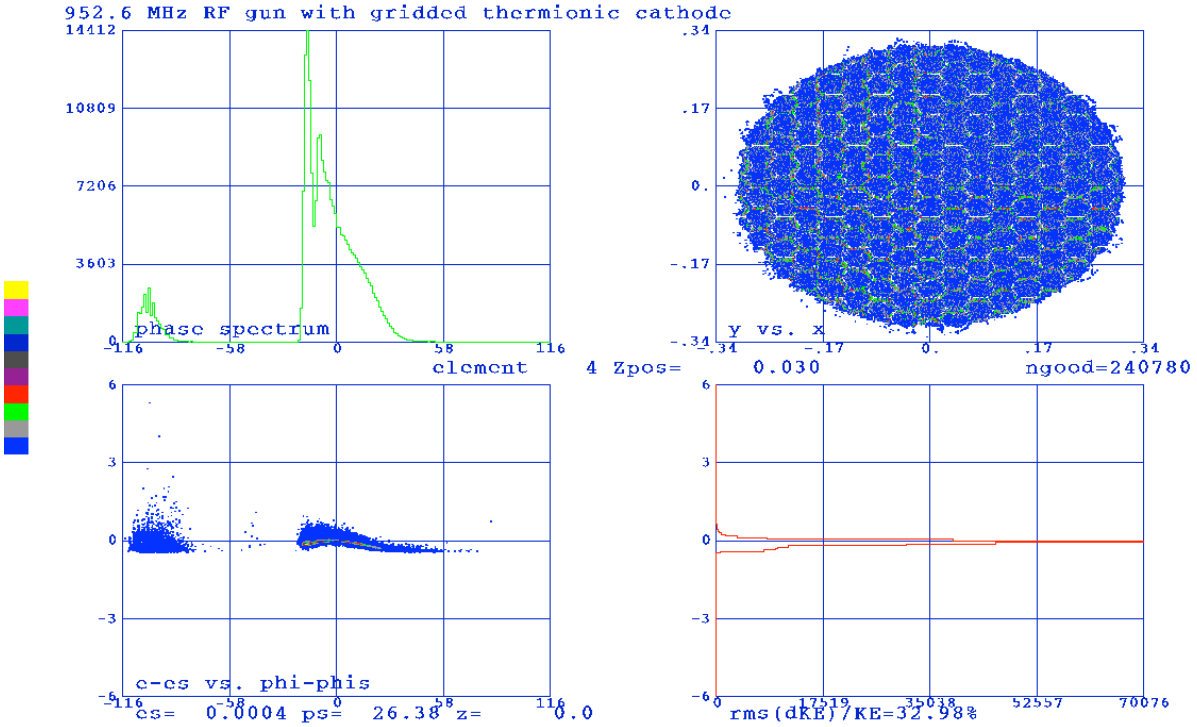

Figure 18 phase and energy spectrum at grid after particles have been removed that hit the grid.

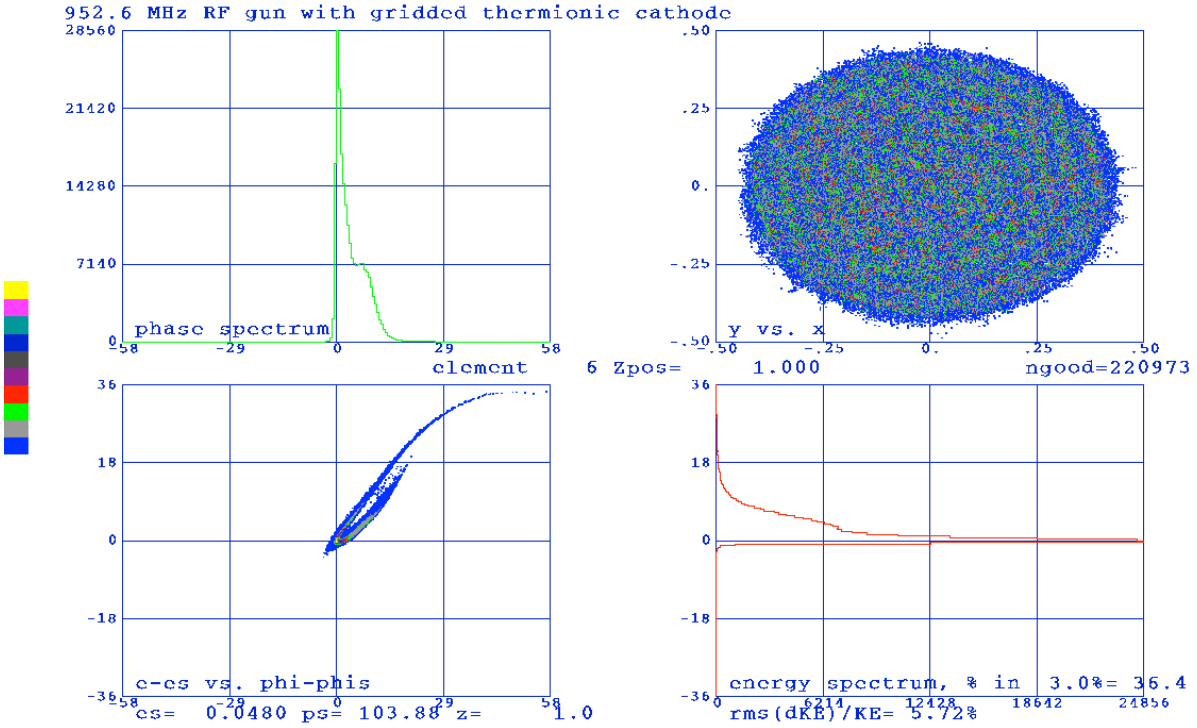

Figure 19 phase and energy spectrum of beam at 1 cm from the cathode. The beam pulse is well formed at this z position.

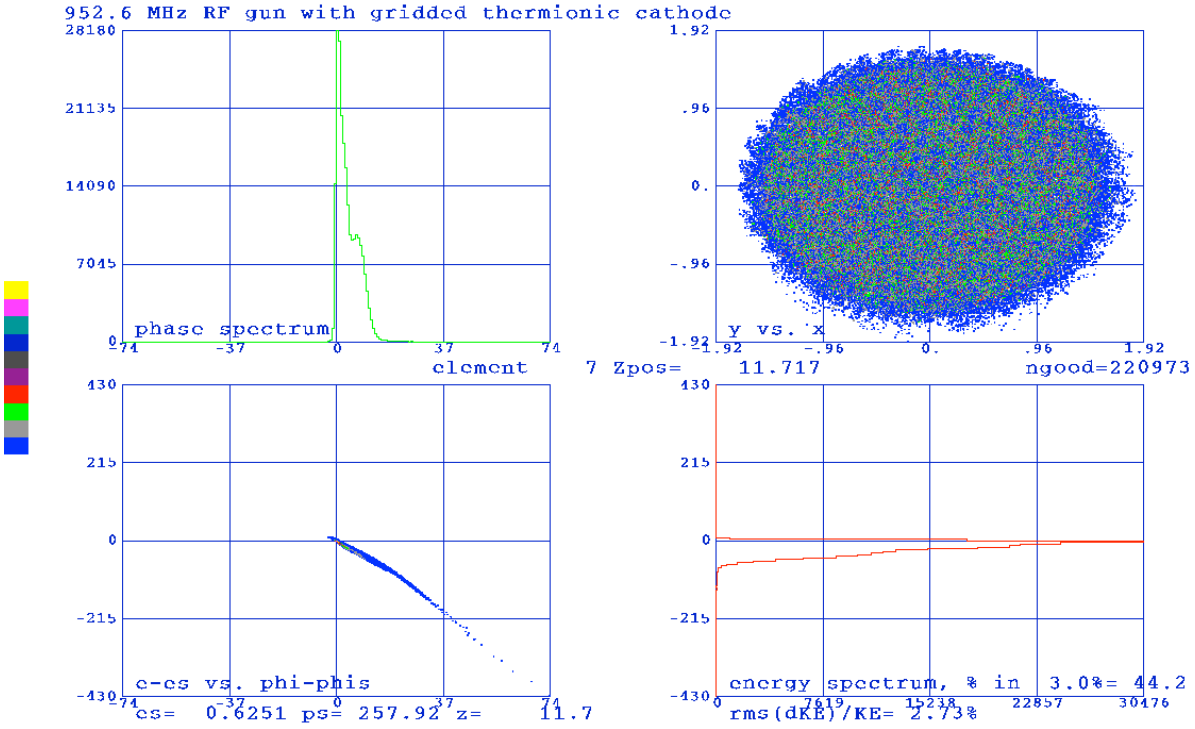

Figure 20 phase and energy spectrum of the beam at the exit of the first superconducting cavity.

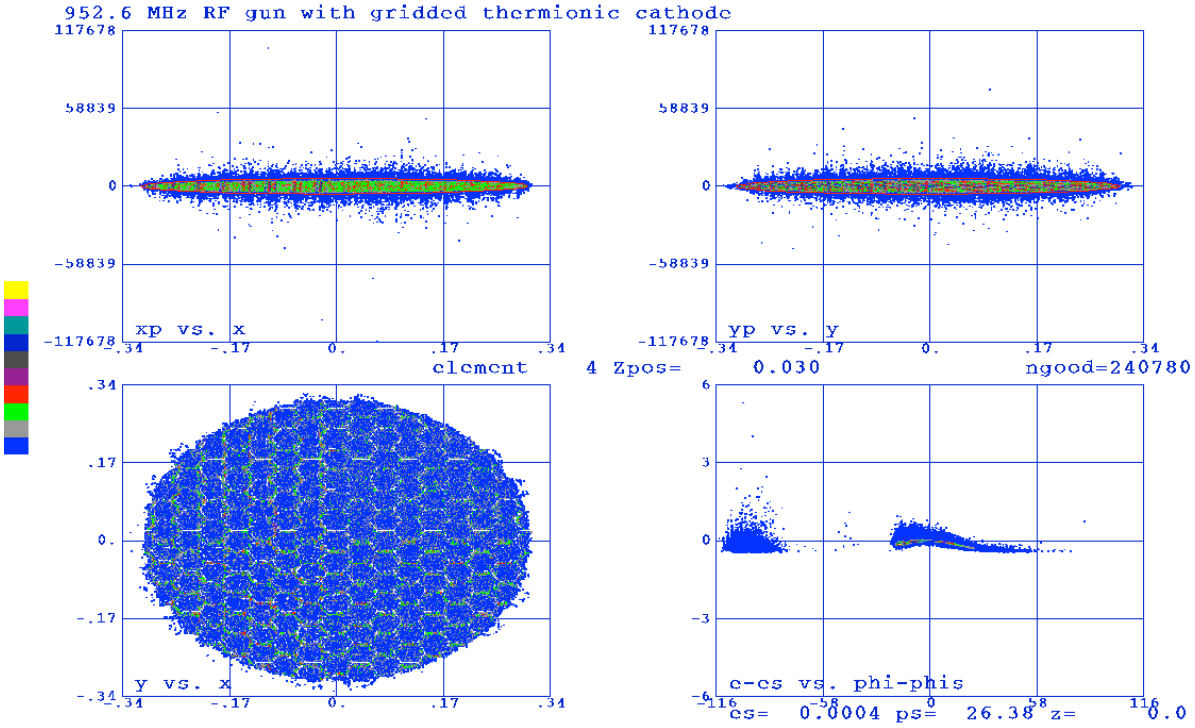

Figure 21 phase space after grid. Note the vertical scales on xp vs x and yp vs x are normally mil-radian, but only for small values of xp. xp=bgx/bgz (beta*gamma in x direction)/beta*gamma in z direction. If bgz is small xp can be very large; same with yp.

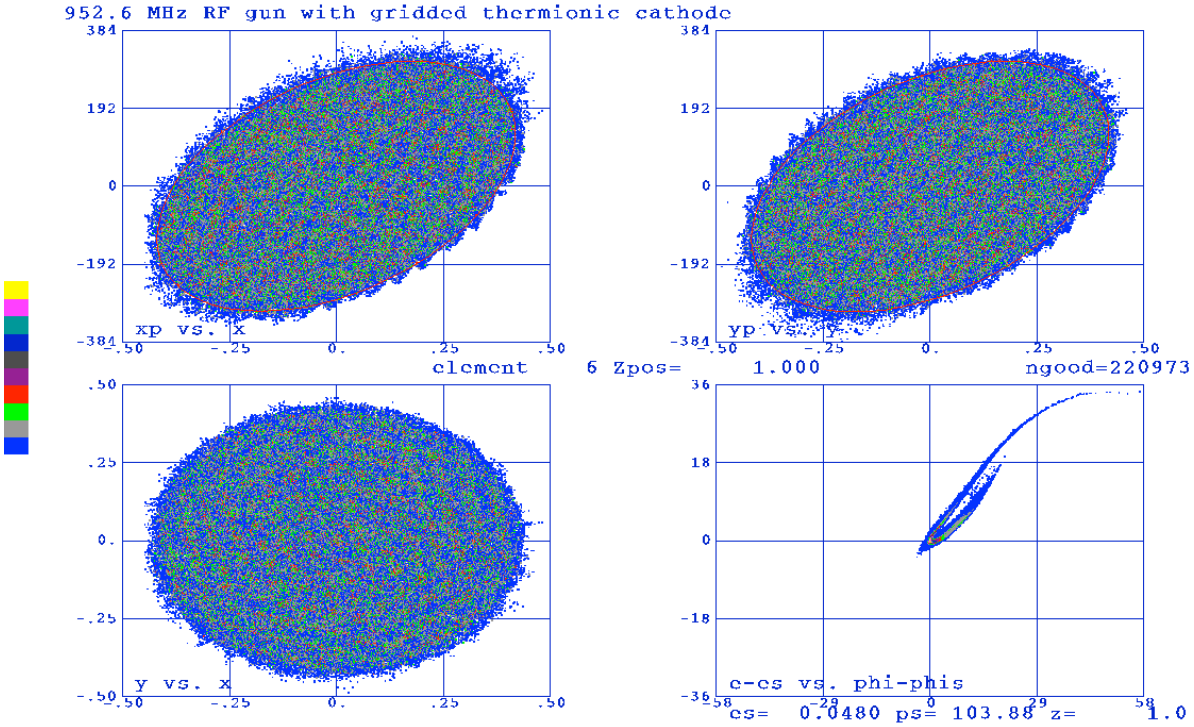

Figure 22 Phase space at 1 cm from cathode. Cathode is immersed in a 2kg magnetic field parallel to the z axis. At 1 cm field is about 600 gauss, beam is now rotating. Thus the emittance is fairly large at ~13cm-mrad normalized.

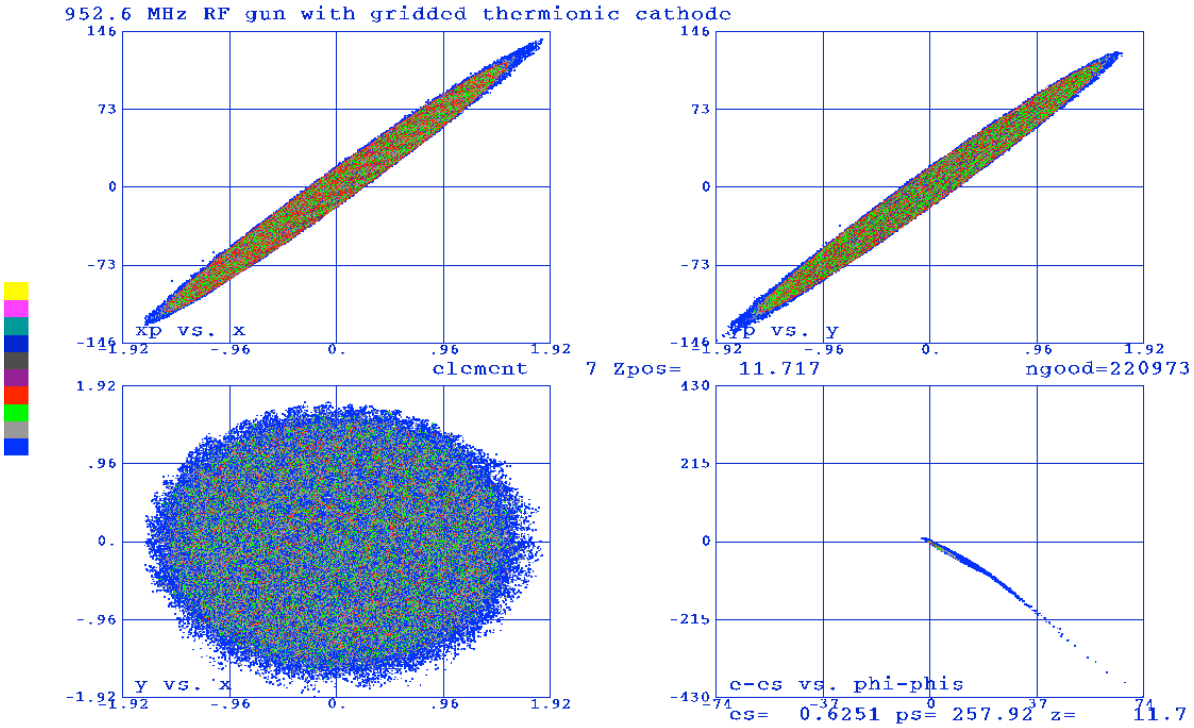

Figure 23 phase space at end of first superconducting cavity.

Thermal Analysis

The thermal model is shown in figure 24. It was developed with 2-D axisymmetric elements, this was necessary at this stage since many runs were required, each with a high complexity of temperature dependent material properties and thermal radiation included. Material thermal conductivity was included for the superconducting materials niobium-titanium and RRR niobium from 2 kelvin to above the critical temperature of each. Stainless steel thermal conductivity was also included from 2K to above room temperature to evaluate the transition section. Helium properties were included as a function of temperature and pressure from 2 kelvin to above room temperature for pressures ranging from one atmosphere to above 3 atmospheres.

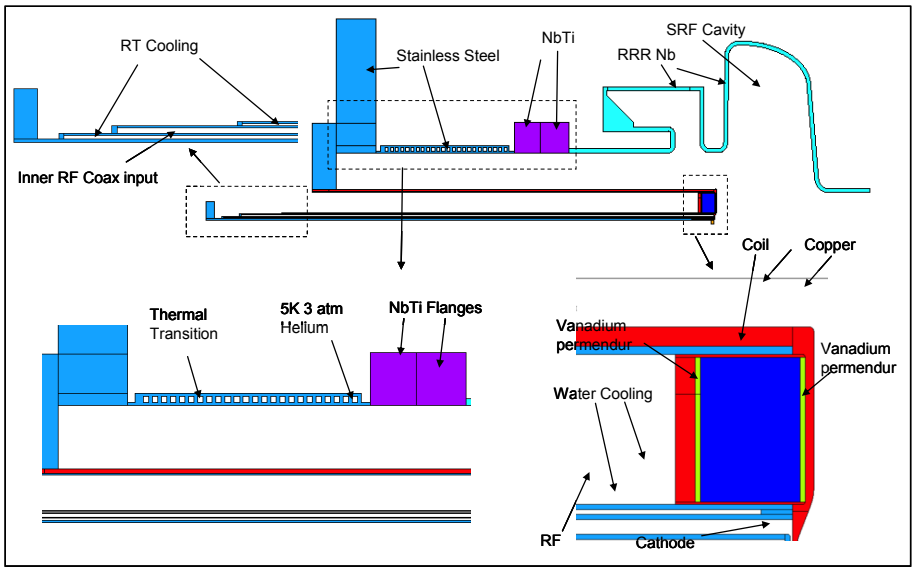

Figure 24, Axisymmetric Thermal Model

Thermal boundary conditions are shown in figure 25. RF heat loads are developed by mapping the magnetic fields from the RF models to the thermal models and determining the surface resistance based on material and surface temperature. This requires the RF losses to be calculated iteratively after a solution is complete and to continue the process until the temperatures are stable. The RF heat loads shown in figure 25 represent the loads at temperature after the solution has converged. Electrical resistivity of each material is input as a set of equations depending on temperature. Cooling was added to the stainless steel room temperature flanges to stabilize the temperature in that region. Heat loads in the inner coax feed that represent two frequencies are determined by calculating the heat loads for each frequency independently and summing them together at an element surface. These heat loads are temperature and frequency dependent. The cathode temperature is set to 1000ºC (1273K). Radiation surface emissivity for copper plated stainless steel was set to .07 and for NbTi and niobium was set at .2. Radiation load into SRF NbTi and Nb totals less than 1 watt. The temperature results are shown in figures 26, 27, and 28.

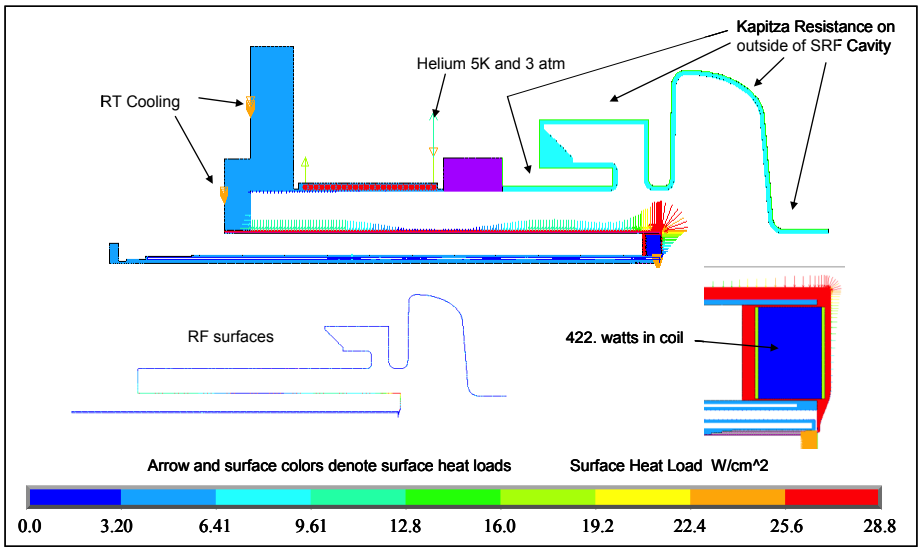

Figure 25, Thermal Model Boundary conditions

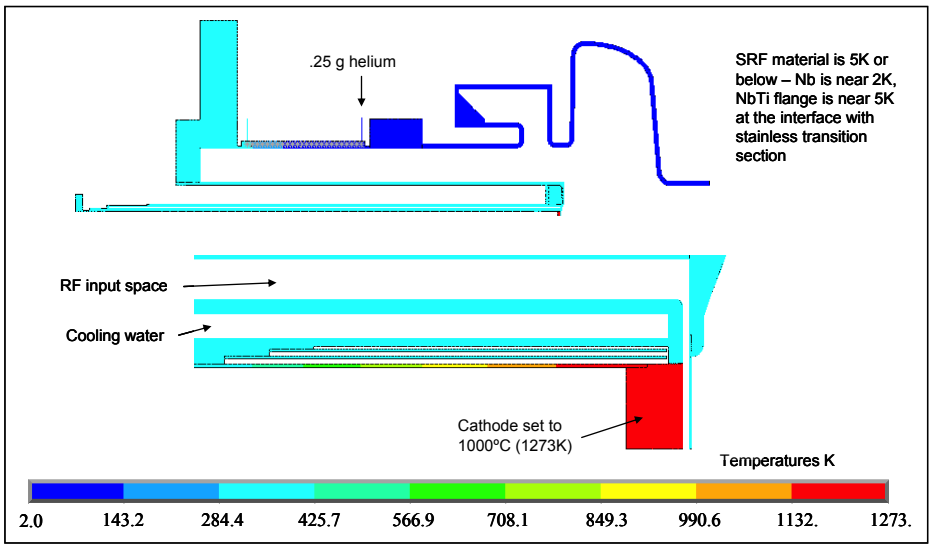

Figure 26, Thermal Model Temperatures

Detail transition section temperatures are shown in figure27. Helium at 5K and 3 atm. was introduced near the NbTi flanges. One quarter of a gram of helium was enough to stabilize the temperatures in this region. Peak temperatures of 354K occur in the stainless steel flanges, shown to the left of the figure. These temperatures can be decreased by locating water coolant near the intersection of the two flanges. In the upper right of the figure the pressure drop of helium is shown. The outlet pressure of 21.8 psi (1.48 atm) leaves enough headroom for the helium system. Figure 28 shows the temperatures of the coil which is located at the cathode end of the stalk. The maximum temperature within the coil is 356K (83ºC). this temperature is well within the limits of the coil materials, copper, kapton, and epoxy.

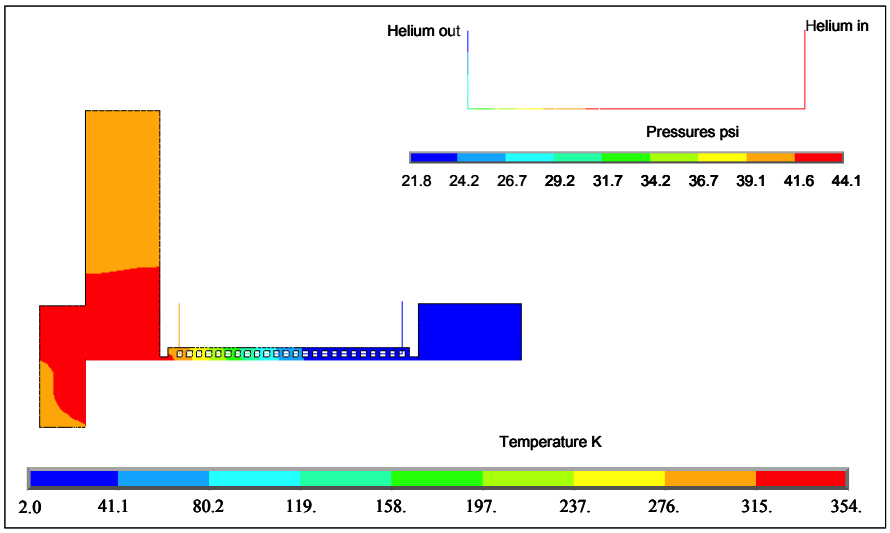

Figure 27, Transition Section Temperatures

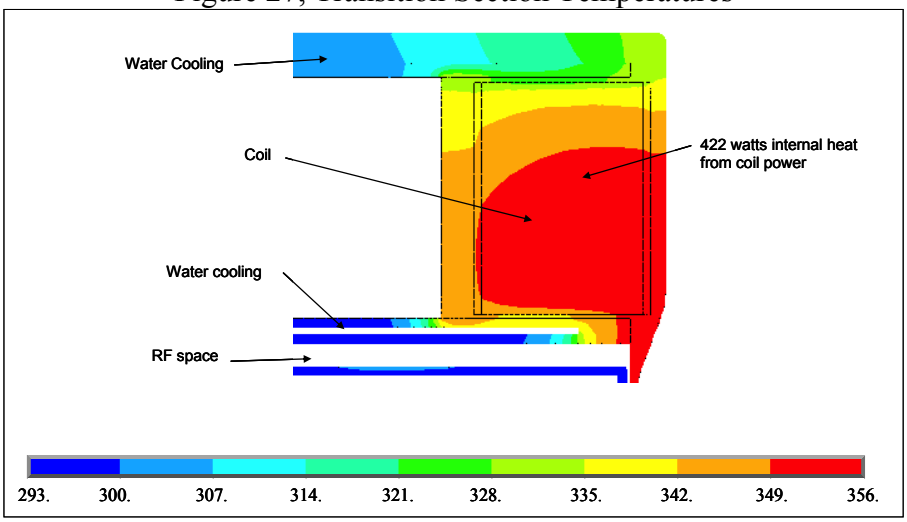

Figure 28, Coil and Stalk End Temperatures

Summary

RF analysis, beam dynamics and thermal analysis show that a thermionic cathode of the design shown here can be embedded within a superconducting cell and produce high current, 400 mA and higher, of beam with good beam quality, 20 mm-mrad rms emittance without magnetization. A small coil made with copper foil can be included in the room temperature stem and produce a solenoid field of 2kGauss on the cathode. Though not shown here, a second cell can be added close to the first cell run at a different phase to decrease energy spread. However, it may be more beneficial to add focusing after the first cell and then a second SRF cell. This can be looked at in Phase II after MEIC has refined its beam requirements.

References

[1] W. Schollkopf, S. Gewinner, W. Erlebach, et al. "The IR and THz Free-Electron Laser at the Fritz-Haber-Institute," Proceedings of the FEL2013, weps062, New York, NY. USA

[2] H. P. Bluem, D. Dowell, A. M .M. Todd, L. M. Young, "High Brightness Thermionic Electron Gun Performance," WG1010, Proceedings of ERL2011, Tsukuba, Japan.

[3] Lewellen, J.W. and Milton, S. "Preliminary Calculations of Ballistic Bunch Compression with Thermionic Cathode RF Guns," Proc. SPIE . Int. Soc. Opt. Eng (Coherent Electron Beam X-Ray Sources: Techniques and Applications), Vol. 3154, pp. 162-171 (1997).

[4] Yuhong Zhang., "The Electron-Ion Collider Project at Jefferson Lab," Seminar at Argonne National Lab July 23, 2013.

[5] Vasiliy Morozov for JLAB's MEIC Study Group, "Update on JLAB MEIC Project," EIC Generic Detector R&D Advisory Committee Meeting, BNL, January 13, 2014.

[6] V. Volkov, E. Kenjebulatov, S. Krutikhin, G. Kurkin, V. Petrov, E. Rotov, N. Vinokurov, "Thermionic cathode-grid assembly simulations for RF Guns," Proc of PAC09, mo6rfp087, Vancouver, BC, Canada.

[7] A. Todd, H. Bluem, V. Christina, M. Cole, D. Dowell, et.al., "High-Performance Aceelerators for Free-Electron Laser (FEL) and Security Applications," THP043, PAC, 2011 New York, NY.

[8] H. Bluem et al., Paper MOPA09, *Proc. FEL 2010*. http://accelconf.web.cern.ch/AccelConf/FEL2010/

[9] W. Schöllkopf, S. Gewinner, W. Eflebach, et.al., "Status of the Frits Haber Institute THZ FEL," TUPB30, *Proc*. *FEL 2011*, Shanghai, China.

[10] P. Sprangle et al., Physical Review Special Topics -Accelerators and Beams **14**, 020702 (2011).

[11] L. M. Young, priv. Comm..

[12] G. R. Neil et al., "The JLAB High-Power ERL Light Source," Nucl. Instr. & Meth. A 557 (2006).

[13] E. J. Minehara, "Development and Operation of the JAERI ERL (Energy Recovery Linac)," ibid.

[14] V. P. Bolotin, N. A. Vinokurov et al., "ERL at Budker INP," ibid.

[15] G. Hoffstaetter et al., "ERL Upgrade of an Existing X-ray Facility: CHESS at CESR," Proc. EPAC 2004, ISBN 92-9083-231-2, Lucerne, Switzerland (2004) 497-499.

[16] M. W. Poole and E. A. Seddon, "4GLS and the Prototype Energy Recovery Linac Project at Daresbury," Proc. EPAC 2004, ISBN 92-9083-231-2, Lucerne, Switzerland (2004) 455-457.

[17] E.-S. Kim et al., "Design Study for a 205 MeV Energy Recovery Linac Test Facility at the KEK," Proc. EPAC 2004, ISBN 92-9083-231-2, Lucerne, Switzerland (2004) 420-422.

[18] I. Ben-Zvi and V. Litvinenko, "ERLs in High Energy and Nuclear Physics," Nucl. Instr. & Meth. A 557 (2006).